

Local Enhancement of Dopant Diffusion from Polycrystalline Silicon  
Passivating Contacts

Peer-reviewed author version

FIRAT, Meric; Wouters, Lennaert; Lagrain, Pieter; Haase , Felix; Polzin, Jana-Isabelle; Chaudhary, Aditya; Nogay, Gizem; Desrues, Thibaut; Krugener, Jan; Peibst, Robby; TOUS, Loic; Radhakrishnan, Hariharsudan Sivaramakrishnan & POORTMANS, Jef (2022) Local Enhancement of Dopant Diffusion from Polycrystalline Silicon Passivating Contacts. In: ACS Applied Materials & Interfaces, 14 (15) , p. 17975 -17986.

DOI: 10.1021/acsami.2c01801

Handle: <http://hdl.handle.net/1942/37591>

# Local Enhancement of Dopant Diffusion from Polycrystalline Silicon Passivating Contacts

Meriç Fırat<sup>a,b,\*</sup>, Lennaert Wouters<sup>b</sup>, Pieter Lagrain<sup>b</sup>, Felix Haase<sup>c</sup>, Jana-Isabelle Polzin<sup>d</sup>, Aditya Chaudhary<sup>e</sup>, Gizem Nogay<sup>f</sup>, Thibaut Desrues<sup>g</sup>, Jan Krügener<sup>h</sup>, Robby Peibst<sup>c,h</sup>, Loic Tous<sup>b</sup>, Hariharsudan Sivaramakrishnan Radhakrishnan<sup>b</sup>, Jef Poortmans<sup>a,b,i</sup>

<sup>a</sup>*KU Leuven, Department of Electrical Engineering, Kasteelpark Arenberg 10, 3001 Leuven, Belgium*

<sup>b</sup>*Imec (Partner in EnergyVille), Kapeldreef 75, 3001 Leuven, Belgium*

<sup>c</sup>*ISFH, Am Ohrberg 1, 31860, Emmerthal, Germany*

<sup>d</sup>*Fraunhofer ISE, Heidenhofstraße 2, 79110, Freiburg, Germany*

<sup>e</sup>*ISC-Konstanz, Rudolf-Diesel-Straße 15, 78467 Konstanz, Germany*

<sup>f</sup>*CSEM, Rue Jacquet-Droz 1, 2002 Neuchâtel, Switzerland*

<sup>g</sup>*Université Grenoble Alpes, CEA, LITEN, DTS, LPA, F-73370 Le Bourget-du-Lac, France*

<sup>h</sup>*Leibniz University Hannover, Institute of Electronic Materials and Devices, Schneiderberg 32, 30167 Hannover, Germany*

<sup>i</sup>*Hasselt University, Campus Diepenbeek, Agoralaan Gebouw D, 3590 Diepenbeek, Belgium*

**Abstract** – Passivating contacts consisting of heavily doped polycrystalline silicon (poly-Si) and ultrathin interfacial silicon oxide (SiO<sub>x</sub>) films enable the fabrication of high-efficiency Si solar cells. The electrical properties and working mechanism of such poly-Si passivating contacts depend on the distribution of dopants at their interface with the underlying Si substrate of solar cells. Therefore, this distribution, particularly in the vicinity of pinholes in the SiO<sub>x</sub> film, is investigated in this work. Technology Computer-Aided Design (TCAD) simulations were performed to study the diffusion of dopants, both phosphorus (P) and boron (B), from the poly-Si film into the Si substrate during the annealing process typically applied to poly-Si passivating contacts. The simulated 2D doping profiles indicate enhanced diffusion under pinholes, yielding deeper semicircular regions of increased doping compared to regions far removed from the pinholes. Such regions with locally enhanced doping were also experimentally demonstrated using high-resolution (5-10 nm/pixel) scanning spreading resistance microscopy (SSRM) for the first time. The SSRM measurements were performed on a variety of poly-Si passivating contacts, fabricated using different approaches by multiple research institutes, and the regions of doping enhancement were detected on samples where the presence of pinholes had been reported in the related literature. These findings can contribute to a better understanding, more accurate modeling, and optimization of poly-Si passivating contacts, which are increasingly being introduced in the mass production of Si solar cells.

**Keywords** – poly-Si passivating contacts, scanning spreading resistance microscopy, pinholes, oxide, dopant diffusion, Sentaurus Process TCAD

## 1 Introduction

The passivating contact technology based on heavily doped polycrystalline silicon (poly-Si) and ultrathin interfacial silicon oxide ( $\text{SiO}_x$ ) films is promising for enhancing the power conversion efficiency of Si solar cells, having enabled efficiencies up to 26.1%<sup>1,2</sup>. Poly-Si passivating contacts have already been introduced in PV manufacturing at the rear side of n-type Si solar cells, and currently yield efficiencies over 24% in mass production<sup>1,3,4</sup>. The main driver of this success is the capability of these passivating contacts to deliver low recombination current densities ( $J_0$ )  $< 5 \text{ fA/cm}^2$  i.e., a high level of passivation, and low contact resistivities ( $\rho_c$ )  $< 5 \text{ m}\Omega\cdot\text{cm}^2$  simultaneously<sup>1,5</sup>. This advantageous property follows from the physical mechanisms governing the transport of charge carriers through the passivating contact<sup>6-8</sup>.

The poly-Si passivating contact structure is illustrated in Fig. 1 for the case of n-type poly-Si. In solar cells, the passivating contact is placed between the monocrystalline Si (c-Si) absorber, where free charge carriers are photogenerated, and the metal contacts, where the carriers are collected<sup>1</sup>. Fabrication of poly-Si passivating contacts normally involves thermal annealing, which can form two features, shown in Fig. 1, that are of importance for the transport of charge carriers: (i) disruptions in the  $\text{SiO}_x$  film called pinholes and (ii) an  $n^+$  ( $p^+$ ), in case of n-type (p-type) poly-Si, region in the substrate, adjacent to the  $\text{SiO}_x$  interface<sup>1,6,9,10</sup>. While the pinholes are formed due to reorganization of the  $\text{SiO}_x$  during annealing, the  $n^+$  ( $p^+$ ) region is the result of dopant diffusion from the poly-Si into the substrate due to the thermal budget of annealing<sup>10,11</sup>. Experimental evidence for both the pinholes and the diffused region is present in the literature<sup>6,10,12-15</sup>.

The function of the passivating contact is to regulate the transport of charge carriers in a selective manner<sup>16,17</sup>. Carrier selectivity has already been defined quantitatively in the literature, and is proportional and inversely proportional to the resistances the minority and majority carriers face, respectively, when being extracted to the contact<sup>18</sup>. Therefore, while transport of the majority carriers, i.e., electrons in Fig.1 for the n-type poly-Si passivating contact, to the metal contact is to be facilitated for achieving a low  $\rho_c$ , transport of the minority carriers is to be blocked to obtain a low  $J_0$ <sup>16,17</sup>. Hence, to minimize the  $J_0$  and  $\rho_c$  by enhancing carrier selectivity, it is important to understand the mechanisms of carrier transport across poly-Si passivating contacts and accurately model the transport based on experimental evidence and data.

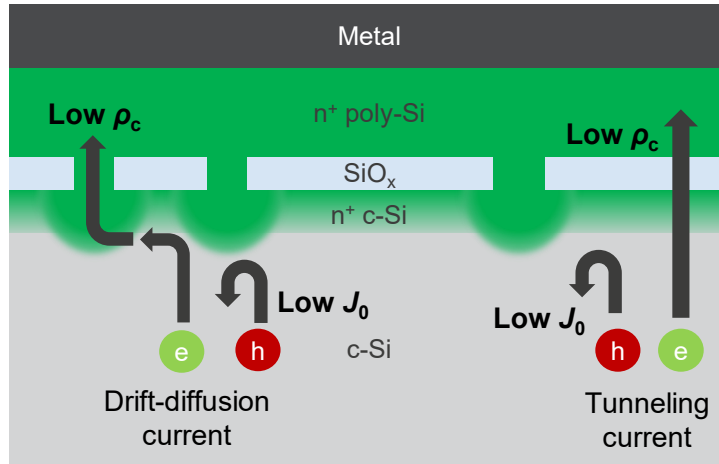


Figure 1. Schematic of the poly-Si passivating contact structure with pinholes in the interfacial oxide film. Unhindered transport of majority carriers i.e., electrons (e) and mitigation of the transport of minority carriers i.e., holes (h) to the metal contact are indicated with arrows, which lead to low  $\rho_c$  and  $J_0$ , respectively. The two carrier transport mechanisms, drift-diffusion through the pinholes and quantum-mechanical tunneling through the oxide are also illustrated.

Multiple studies have already been devoted to identifying the carrier transport mechanisms of poly-Si passivating contacts. The current state of understanding based on these studies suggests that carrier transport occurs by two possible mechanisms, which can be active simultaneously: quantum-mechanical tunneling across the  $\text{SiO}_x$  film and drift-diffusion via the pinholes in the  $\text{SiO}_x$  film (see Fig. 1). The transport model based on tunneling was first proposed by the bipolar junction transistor community to explain the transistor gain enhancement observed when using a poly-Si emitter<sup>12,19</sup>. Subsequently, evidence of tunneling being the dominant transport mechanism for poly-Si passivating contact designs with sufficiently thin ( $< 2$  nm) and intact  $\text{SiO}_x$  films has also been reported by PV researchers<sup>8,20,21</sup>. In the tunneling model, the carrier selectivity is a result of electrons facing a lower energy barrier height for tunneling than holes<sup>7,19</sup>. This, however, only explains the selectivity in case of n-type but not p-type poly-Si passivating contacts<sup>7</sup>, even though the latter can also yield excellent properties in terms of  $J_0$  and  $\rho_c$ <sup>5</sup>. Due to this discrepancy of the tunneling model, the pinhole transport model was proposed, which is based on the aforementioned experimental evidence indicating the presence of pinholes in the interfacial  $\text{SiO}_x$  film<sup>6,7,22</sup>. After the introduction of this model, several researchers have reported that pinhole transport is the dominant mechanism in passivating contacts annealed at temperatures high enough to induce a relatively high density of pinholes<sup>20,21,23,24</sup>. In contrast to the tunneling model, the pinhole model can explain the carrier selectivity of both n- and p-type poly-Si passivating contacts, as the selectivity arises from the presence of nanosized high-low or p-n junctions in the substrate under the pinholes<sup>7</sup>. These junctions

exhibit band bending favorable for majority and unfavorable for minority carrier transport, thereby inducing selectivity for electrons (n-type doping) or holes (p-type doping) <sup>16,17</sup>.

Based on the observation that tunneling and pinhole transport may coexist and could both potentially be the dominant means of transport depending on the SiO<sub>x</sub> film properties such as thickness <sup>20,21</sup>, a model superposing the two mechanisms was proposed, which can explain experimentally determined  $J_0$  and  $\rho_c$  values for various types of poly-Si passivating contacts <sup>6</sup>. Subsequently, this combined model was refined and implemented by various groups for investigating, predicting, and optimizing the properties of poly-Si passivating contacts <sup>25–27</sup>. While these implementations are powerful tools, they still rely on a few simplifying assumptions. One common assumption of the models implemented is that the diffused region in the substrate is homogeneous <sup>25–27</sup>. However, process simulation studies have shown for both phosphorus (P)- and boron (B)-doped poly-Si passivating contacts that local enhancement of dopant diffusion is expected in the substrate under the pinholes, as depicted schematically in Fig. 1 <sup>10,28</sup>.

Given the importance of the local high-low or p-n junctions under the pinholes for the selectivity mechanism of the pinhole transport model, accurately representing these junctions in the implemented models is desirable. However, the doping concentration in these junctions is unexplored and hardly accessible due to the lack of conventional experimental techniques for two-dimensional (2D) dopant distribution measurements <sup>7</sup>. An interesting investigation by scanning Kelvin probe microscopy (SKPM) was reported, where the poly-Si and SiO<sub>x</sub> films (1.5 or 2.2 nm thick) of the passivating contact as well as 125-250 nm of the diffused region in the Si substrate were etched away and subsequent SKPM measurements revealed surface potential non-uniformities of < 500 nm in width, which were interpreted as indicators of doping non-uniformities <sup>29</sup>. Nevertheless, it remains desirable to investigate the dopant distribution by a technique which does not involve layer removal for increased accuracy and allows the assessment of the dopant concentration in cross-section, which is not accessible by SKPM.

In this work, this research gap is addressed by a study of the dopant distribution in the substrate under poly-Si passivating contacts and particularly in the vicinity of pinholes, both by simulations and experiments. First, Technology Computer-Aided Design (TCAD) simulations are performed using the Sentaurus Process software to investigate how the annealing process influences the dopant diffusion from the poly-Si into the substrate, through the SiO<sub>x</sub> and via

pinholes. The impact of annealing temperature ( $T_{\text{ann}}$ ), pinhole size ( $d_{\text{pin}}$ ), and dopant type on the resulting 2D dopant distribution is assessed. Subsequently, the cross-sectional dopant distribution is also investigated experimentally using scanning spreading resistance microscopy (SSRM), which is a technique capable of acquiring cross-sectional 2D resistance ( $R$ ) and active dopant concentration ( $N_{\text{act}}$ ) maps at a sufficiently high resolution to visualize the local non-uniformities in doping level surrounding the pinholes<sup>30</sup>. To our best knowledge, this is the first time such information is made accessible to the research community. The SSRM analysis is performed on various poly-Si passivating contact structures, to study the impact of multiple design and process parameters on the dopant distribution under the passivating contacts and the pinholes. The varied parameters include the  $\text{SiO}_x$  growth method and thickness ( $t_{\text{ox}}$ ), the type of dopant added to the poly-Si film, the substrate surface morphology, and the  $T_{\text{ann}}$ . The information acquired by the study advance the understanding of the working principle of poly-Si passivating contacts. The findings can enable improved accuracy of the models of the passivating contacts, which could facilitate further optimization of their selectivity.

## 2 Materials and Methods

### 2.1 Sentaurus Process TCAD Simulations

The Sentaurus Process software provided by Synopsys was used to perform TCAD simulations of the annealing process which is typically applied to poly-Si passivating contacts. The simulations were performed using a 2D model of the passivating contact in cross-section, which consists of three layers: (i) a  $1\ \mu\text{m} \times 1\ \mu\text{m}$  Si substrate with P or B doping of a concentration of  $1.66 \cdot 10^{15}\ \text{cm}^{-3}$ , (ii) an interfacial  $\text{SiO}_x$  layer with a fixed  $t_{\text{ox}} = 1.5\ \text{nm}$  and a centrally located pinhole with  $d_{\text{pin}} = 2\text{-}20\ \text{nm}$ , and (iii) a poly-Si layer of a fixed thickness ( $t_{\text{Si}}$ ) of  $150\ \text{nm}$ , doped with the same dopant as the substrate. For all simulated layers, default material parameters were selected from the Sentaurus Process database using the “Advanced Calibration” setting, unless otherwise mentioned. The model was created starting with the generation of the substrate and the  $\text{SiO}_x$  layers without simulating the oxidation process. Subsequently, the pinhole was defined by etching the  $\text{SiO}_x$  layer locally, using a mask. Afterwards, the structure was completed with the deposition of the poly-Si layer. Hence, the pinhole was filled with poly-Si in the simulated structures. Doping of the poly-Si layer was not simulated but a homogeneous total dopant concentration ( $N_{\text{D}}$  or  $N_{\text{A}}$ ) of  $4 \cdot 10^{20}\ \text{cm}^{-3}$  and  $6 \cdot 10^{19}\ \text{cm}^{-3}$  was chosen for P and B-doped poly-Si layers, respectively, based on experimentally determined values in the literature<sup>31,32</sup>. The choice of dopant concentrations in the poly-Si, the

resistivity of the substrate, and the film thicknesses used in the 2D model described above were based on the design of some of the samples used in the experimental portion of this work. The  $d_{\text{pin}}$  values were selected according to the pinhole diameter values reported in the literature<sup>33</sup>. Moreover, the Arrhenius parameterizations of the diffusivity ( $D^*$ ) of P and B in the  $\text{SiO}_x$  layer were not chosen based on the Advanced Calibration setting. Instead, the default parameterizations from the default calibration setting were used, which read  $7.6 \cdot 10^{-3} \cdot \exp(-3.5 \text{ eV}/kT) \text{ cm}^2/\text{s}$  and  $3.16 \cdot 10^{-4} \cdot \exp(-3.53 \text{ eV}/kT) \text{ cm}^2/\text{s}$  for P and B, respectively, where  $k$  is the Boltzmann constant and  $T$  is the absolute temperature in kelvins (K)<sup>34,35</sup>.

After the creation of the 2D structure, the annealing process was simulated, consisting of three steps: ramp up, anneal, and ramp down. The anneal step was at a constant temperature ( $T_{\text{ann}}$ ), which was selected between  $900^\circ\text{C}$  and  $1035^\circ\text{C}$  and was 30 min long. The starting temperature of the ramp up and the final temperature of the ramp down were both  $800^\circ\text{C}$ . The temperature ramp rates were  $+5^\circ\text{C}/\text{min}$  and  $-3.3^\circ\text{C}/\text{min}$  for the ramp up and ramp down steps, respectively. These annealing parameters were selected based on some of the experimental annealing processes used in this work. Following the simulation of the annealing process, the cross-sectional 2D map of  $N_{\text{act}}$  ( $N_{\text{D,act}}$  for P doping and of  $N_{\text{A,act}}$  for B doping) was generated and qualitatively analyzed.

In addition to the above set of simulations, two further simulations were performed to compare the results with experimentally determined  $N_{\text{act}}$  data for two specific samples. To accurately model the properties of these samples, the simulation parameters were modified. A B-doped substrate with a concentration of  $1.14 \cdot 10^{16} \text{ cm}^{-3}$  was used,  $t_{\text{ox}}$  was 2.2 nm,  $t_{\text{Si}}$  was 225 nm,  $T_{\text{ann}}$  was  $1035^\circ\text{C}$ , and the total dopant concentration in the poly-Si was  $N_{\text{D}} = 6 \cdot 10^{20} \text{ cm}^{-3}$  and  $N_{\text{A}} = 4 \cdot 10^{19} \text{ cm}^{-3}$  for P- and B-doped layers, respectively.

## 2.2 SSRM Measurements

### 2.2.1 Sample Design and Preparation

For the experimental investigation by the SSRM method, samples were prepared at 5 different research institutes. The samples share a similar structure consisting of a c-Si substrate, a thin  $\text{SiO}_x$  film, a heavily doped poly-Si film and, for some samples, a silicon nitride ( $\text{SiN}_x$ ) film on top, with all layers covering the full sample area. The fabrication process also consists of similar steps for all samples. A c-Si wafer was treated with a process defining its surface

morphology such as polishing or texturing, which was followed by oxidation and the deposition of a Si film, either in amorphous or polycrystalline form. The Si films were either *in situ* doped during film growth or *ex situ* doped in a separate step. Subsequently, thermal annealing was performed, during which, among other structural modifications, the Si films deposited in amorphous state crystallize to poly-Si. In addition, SiN<sub>x</sub> was deposited on a few of the samples. Samples with SiN<sub>x</sub> were also subsequently fired, which is a rapid thermal annealing process performed in a belt furnace. The thermal budget of firing is significantly lower than that of annealing, therefore, the firing process is not expected to significantly alter the dopant distribution in the Si substrate adjacent to the passivating contact.

Despite sharing an overall similar structure, the samples were prepared with differences in certain design and process parameters to study the impact of these on the dopant distribution under the passivating contact. These parameters are: (i) the surface morphology of the substrate (polished, saw-damage removed (SDR), or random pyramid textured (RPT)), (ii) the method used for growing the SiO<sub>x</sub> film, (iii) the  $t_{ox}$ , (iv) the type and concentration of active dopants incorporated in the Si film, and (v) the annealing thermal budget indicated by the  $T_{ann}$  and the annealing duration ( $t_{ann}$ ). For each sample used in this work, the values of these parameters are shown in Table 1. The  $t_{ox}$  values were measured by transmission electron microscopy (TEM) in case of samples Imec-A-D and by spectroscopic ellipsometry otherwise. The  $N_{act}$  values were determined by Hall measurements in case of samples Imec-A-D and by electrochemical capacitance-voltage (ECV) measurements otherwise. Other differences between the samples, which are not considered significant for the distribution of dopants, are listed in Table S1, in the Supporting Information.

Table 1. The most relevant design and process parameters of the samples used in this study.

Name	Substrate Surface Morphology	SiO <sub>x</sub> Growth Method	$t_{ox}$	Dopant Type	Dopant Concentration	Annealing Thermal Budget
Imec-A	Polished	Thermal	1.5 nm	P	$1.5 \cdot 10^{20} \text{ cm}^{-3}$	900°C 30 min
Imec-B						950°C 30 min
Imec-C						1050°C 30 min
Imec-D	RPT					950°C 30 min



CEA	SDR	Thermal (grown in H <sub>2</sub> O:O <sub>3</sub> & thermalized at 580°C)	1.5 nm	P	4·10 <sup>20</sup> cm <sup>-3</sup>	975°C 30 min
ISE	Polished	Thermal	1.2 nm	P	2.5·10 <sup>20</sup> cm <sup>-3</sup>	900°C 10 min
ISFH-A	Polished	Thermal	2.2 nm	P	2.5·10 <sup>20</sup> cm <sup>-3</sup>	1035°C 60 min
ISFH-B				B	3·10 <sup>19</sup> cm <sup>-3</sup>	
ISFH-C	SDR	Wet-chemical (in H <sub>2</sub> O:O <sub>3</sub> )	1.7 nm	P	3.5·10 <sup>20</sup> cm <sup>-3</sup>	840°C 30 min
ISC	SDR	Wet-chemical (in HNO <sub>3</sub> )	1.4 nm	P	2.5·10 <sup>20</sup> cm <sup>-3</sup>	825°C 30 min

In addition to the design and process parameters in Table 1 and Table S1, further information about the samples is summarized in Table 2, which shows the recombination current density ( $J_0$ ) at an injection level of 10<sup>16</sup> cm<sup>-3</sup>, before and after hydrogenation, and the contact resistivity ( $\rho_c$ ) of each passivating contact, along with publication references for the data, where available. Low  $J_0$ , particularly after hydrogenation, of < 5 fA/cm<sup>2</sup> and  $\rho_c$  < 20 mΩ·cm<sup>2</sup> were simultaneously achieved with most samples, indicating that these were processed with optimum or near-optimum conditions determined by each institute where the samples originate. Further details concerning  $\rho_c$  measurements, which differ from sample to sample and can influence the result, are provided in Table S2, in the Supporting Information.

Table 2. Recombination current density ( $J_0$ ) obtained before and after hydrogenation, and contact resistivity ( $\rho_c$ ) of the passivating contact samples listed in Table 1.

Name	$J_0$ – No Hydrogenation	$J_0$ – After Hydrogenation	$\rho_c$	Reference
Imec-A	18.5 fA/cm <sup>2</sup>	-	Non-Ohmic	21
Imec-B	16.4 fA/cm <sup>2</sup>	0.8±0.5 fA/cm <sup>2</sup>	29±2 mΩ·cm <sup>2</sup>	21
Imec-C	High	-	16±1 mΩ·cm <sup>2</sup>	21
Imec-D	25.4 fA/cm <sup>2</sup>	2.4±0.6 fA/cm <sup>2</sup>	18±2 mΩ·cm <sup>2</sup>	21
CEA	20.3 fA/cm <sup>2</sup>	10.7 fA/cm <sup>2</sup>	-	Unpublished
ISE	9.9±1.9 fA/cm <sup>2</sup>	2.0±0.8 fA/cm <sup>2</sup>	4 mΩ·cm <sup>2</sup>	36
ISFH-A	6.2 fA/cm <sup>2</sup>	0.9 fA/cm <sup>2</sup>	0.6±0.2 mΩ·cm <sup>2</sup>	37
ISFH-B	8.7 fA/cm <sup>2</sup>	3.0 fA/cm <sup>2</sup>	0.2±0.1 mΩ·cm <sup>2</sup>	37
ISFH-C	14 fA/cm <sup>2</sup>	4.2 fA/cm <sup>2</sup>	1.3 mΩ·cm <sup>2</sup>	Unpublished
ISC	-	4.6±0.5 fA/cm <sup>2</sup>	1.3±0.1 mΩ·cm <sup>2</sup>	38

To prepare the samples listed in Table 1 for the SSRM measurements, a 500 nm thick protective SiO<sub>2</sub> layer was deposited at 150°C on top of the passivating contact and the samples were cleaved to obtain fresh cross-sections. The cross-sections of the samples were polished with diamond and aluminum oxide lapping films to obtain a surface with a root mean square

roughness less than 250 picometers. Subsequently, the back contact of the sample was made  $\sim 5$  mm away from the polished cross-section, by applying conductive silver paint between the sample and the conductive chuck of the SSRM equipment.

### 2.2.2 Sample Characterization

The SSRM measurements were performed utilizing a Bruker Dimension Icon AFM system with a Nanoscope V controller and an SSRM logarithmic amplifier, in a glove box with Ar environment<sup>30</sup>. The AFM system was equipped with an Imec heavily boron doped diamond probe mounted on a cantilever with a nominal spring constant of 7 N/m<sup>39</sup>. The SSRM measurement setup is schematically depicted in Fig. 2a). To acquire a 2D  $R$  map of the SSRM sample under test, the AFM probe was scanned across the polished cross-section and  $R$ , normally dominated by the spreading resistance between the probe and the sample, was measured throughout the scan. The scans were performed using a force of 5-20  $\mu$ N and a bias voltage of -0.5 V. The  $R$  maps were collected at a resolution of 5-10 nm/pixel and a scan rate of 1 Hz. In all  $R$  maps, the logarithm of  $R$  is depicted.

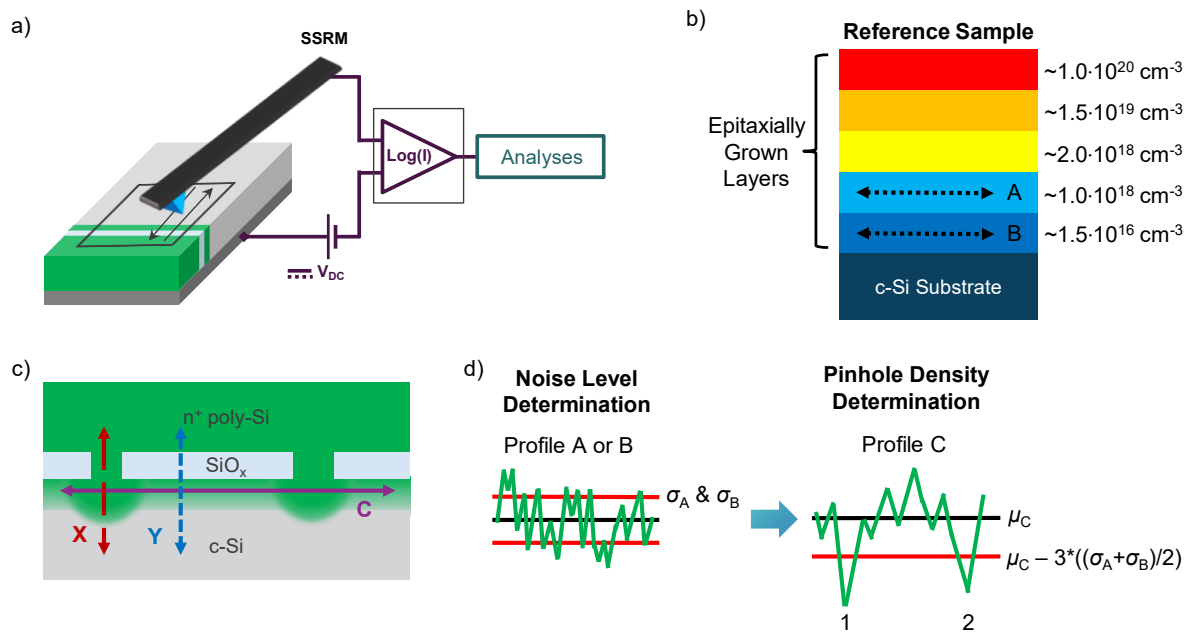


Figure 2. a) Schematic of the scanning spreading resistance microscopy (SSRM) setup for 2D resistance ( $R$ ) mapping measurements. b) Schematic of a calibration sample with epitaxially grown layers of different and known doping level, used for converting  $R$  maps to  $N_{\text{act}}$  maps. The dotted arrows indicate the locations where horizontal 1D profiles A and B of  $R$  were extracted for determining the measurement noise. c) Schematic of the cross-section measured by SSRM. Arrow C indicates the location where a horizontal 1D  $R$  profile is extracted for determining the density of regions with enhanced dopant diffusion. Arrows X and Y indicate the locations of vertical 1D profiles extracted for determining the active dopant concentration ( $N_{\text{act}}$ ) across the passivating contact. d) Drawing indicating the extraction of noise level from the profiles A and B shown in b), and the estimation of the number of regions with enhanced diffusion from the profile C. The symbols  $\mu$  and  $\sigma$  stand for the mean and standard deviation values of the respective profiles. Where  $R$  drops by  $3\sigma$  below  $\mu$ , a pinhole is deemed to be present, indicated as “1” and “2” in the schematic example in d).

The 2D  $R$  maps were further converted to  $N_{\text{act}}$  maps using c-Si calibration samples with epitaxially grown layers of different  $N_{\text{act}}$  levels, as illustrated in Fig. 2b). The  $N_{\text{act}}$  levels on the calibration samples were measured precisely by spreading resistance profiling. The 2D  $R$  maps acquired by SSRM on the calibration samples were used for determining the relationship between  $R$  and  $N_{\text{act}}$ , which was applied for determining the  $N_{\text{act}}$  map of the sample under test.

From the 2D  $R$  maps, horizontal 1D  $R$  profiles were extracted just under the interfacial  $\text{SiO}_x$  film (see Profile C in Fig. 2c)). Regions with local minima in  $R$ , which indicate locally enhanced dopant diffusion, were identified and the shape and size of the identified regions were assessed. In particular, the radii of the regions ( $r_{\text{diff}}$ ) were measured, defined as the distance between the  $\text{SiO}_x$  interface and the position where the base resistance of the substrate is reached.

When a significant number ( $\geq 4$ ) of regions with enhanced dopant diffusion were detected in a single  $R$  map, the density of the regions was also estimated. The entire procedure used for this purpose is explained in Fig. 2. The density estimation was performed using the 1D  $R$  profile shown in Fig. 2c) as Profile C, which covers the entire width of the 2D  $R$  map. To quantitatively identify the regions of enhanced diffusion in Profile C, regions with  $R$  values lower than the mean  $R$  value of Profile C ( $\mu_C$ ) by at least 3 times the noise level ( $\sigma$ ) were considered (see Fig. 2d)). For determining the noise level, Profiles A and B were acquired across the two epitaxial layers of the calibration sample with  $R$  just above and below the range of  $R$  values observed in Profile C, and the average of their standard deviations  $\sigma_A$  and  $\sigma_B$  were taken (see Fig. 2b)). The 1D density was determined by dividing the number of identified regions in Profile C by the width of the  $R$  map. Assuming an equal density of regions in the in-plane direction, the areal density of the regions was calculated as the square of the 1D density.

In addition, the 2D  $N_{\text{act}}$  maps were further analyzed by extracting vertical 1D  $N_{\text{act}}$  profiles across the poly-Si passivating contact structure, in regions both with and without local enhancement of dopant diffusion. These 1D profiles are illustrated in Fig. 2c) as Profiles X and Y. All extracted profiles were averages taken over 5 scan lines i.e., over 5 pixels in the 2D maps. In addition, for comparison with the data acquired by SSRM, 1D profiles of  $N_{\text{act}}$  across selected passivating contacts were also acquired by ECV.

### 3 Setaurus Process TCAD Simulations of the Annealing Process

The thermal annealing process typically applied to poly-Si passivating contacts was simulated using the Setaurus Process TCAD software for an explorative study on the diffusion of dopants from the poly-Si film into the substrate during annealing, both through the SiO<sub>x</sub> film and via pinholes therein. The focus of the study was to assess the impact of three parameters on the 2D distribution of active dopants under the passivating contact: (i)  $T_{\text{ann}}$ , (ii) dopant type, being either P or B, and (iii)  $d_{\text{pin}}$ . The findings of the simulations are summarized in Fig. 3. While  $N_{\text{act}}$  values are shown in Fig. 3, we would like to note that these might be inaccurate due to the simplicity of the model used for performing this qualitative study. In particular, accurate quantitative simulation of dopant diffusion through the SiO<sub>x</sub> layer is challenging, as there is a significant variation in the reported diffusivity parameterizations of dopants, particularly of P, in SiO<sub>x</sub><sup>34</sup>. This is because the diffusivity in SiO<sub>x</sub> depends strongly on multiple parameters such as the growth method and the thermal history of the SiO<sub>x</sub> layer<sup>35</sup>. Hence, a quantitative simulation study would require accurate characterization of the diffusivity by dedicated experiments, which is beyond the scope of this work. In addition, the impact of the annealing process on the SiO<sub>x</sub> integrity, stoichiometry and structure are not considered.

The impact of  $T_{\text{ann}}$  on the distribution of dopants is evident from Fig. 3a)-c), which show the simulation results for a P-doped poly-Si layer and a SiO<sub>x</sub> layer containing a pinhole with  $d_{\text{pin}} = 5$  nm, for  $T_{\text{ann}}$  of a) 900°C, b) 950°C, and c) 1035°C, respectively. These reveal that (i) a semicircular region with enhanced diffusion of dopants with an increased peak concentration and depth is expected under the pinhole, (ii) the radius of this region increases with  $T_{\text{ann}}$ , and (iii) the peak concentration and depth of the diffused dopants far from the pinhole under the intact SiO<sub>x</sub> increase with  $T_{\text{ann}}$  as well. These findings are in good agreement with the results reported by Krügener et. al.<sup>28</sup>, and are due to the temperature dependence of the diffusivity of P. Simulations with B-doped poly-Si but otherwise identical conditions led to the same conclusions and the corresponding results are therefore not all shown here.

Comparison of Fig. 3c) and 3d), which show the simulation results for P- and B-doped poly-Si,  $d_{\text{pin}} = 5$  nm, and  $T_{\text{ann}} = 1035^\circ\text{C}$ , reveals that in case of B doping, the difference between the depth of the diffused profiles under the pinhole and under the SiO<sub>x</sub> film far from the pinhole is lower. In fact, all simulation results with B-doped poly-Si indicate a less pronounced enhancement of dopant diffusion via the pinhole compared to P-doped poly-Si. This is attributed to a smaller difference between B diffusivities in the SiO<sub>x</sub> and Si than in the case of

P. These findings suggest that experimental identification of the regions with enhanced dopant diffusion under pinholes might be more challenging in case of B-doped poly-Si passivating contacts. This conclusion applies particularly for high  $T_{\text{ann}}$ , as this leads to substantial dopant diffusion through the  $\text{SiO}_x$ .

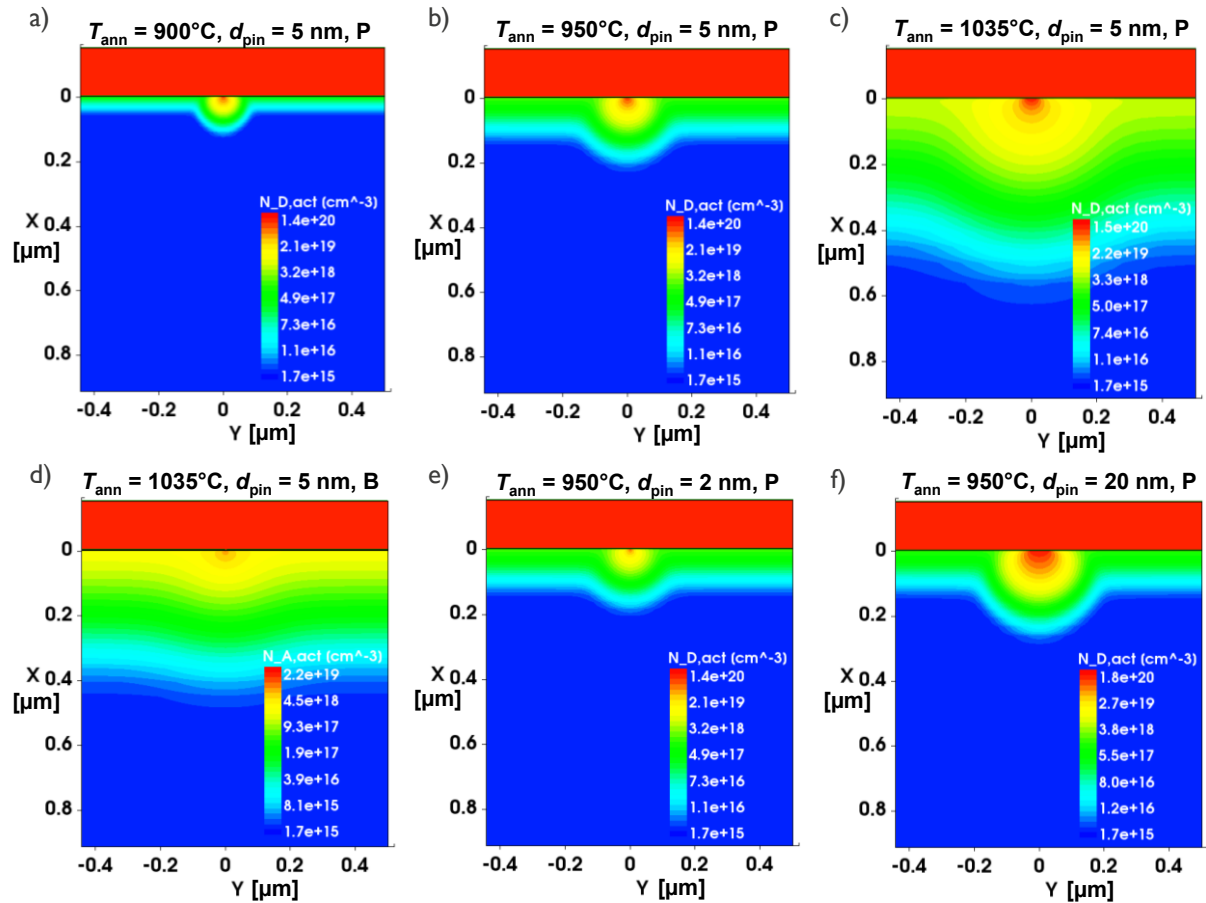


Figure 3. Results of Sentaurus Process TCAD simulations of thermal annealing applied to a 150 nm poly-Si (top) / 1.5 nm  $\text{SiO}_x$  / 1  $\mu\text{m}$  Si (bottom) structure with a centrally located pinhole in the  $\text{SiO}_x$  layer. a), b), c) 2D active phosphorus (P) concentration ( $N_{\text{D,act}}$ ) maps with P-doped poly-Si, pinhole width ( $d_{\text{pin}}$ ) of 5 nm, and annealing temperatures ( $T_{\text{ann}}$ ) of a) 900°C, b) 950°C, and c) 1035°C. d) 2D active boron (B) concentration ( $N_{\text{A,act}}$ ) map with B-doped poly-Si,  $d_{\text{pin}} = 5$  nm, and  $T_{\text{ann}} = 1035^\circ\text{C}$ . e), f) 2D  $N_{\text{D,act}}$  maps with P-doped poly-Si,  $T_{\text{ann}} = 950^\circ\text{C}$ , and  $d_{\text{pin}}$  of e) 2 nm, and f) 20 nm. The legends indicate the active dopant concentration values.

The impact of  $d_{\text{pin}}$  on dopant diffusion via the pinhole was also investigated, as experimental data from the literature suggests that pinholes can have a wide range of widths<sup>33</sup>, and since a similar Sentaurus Process simulation study found that a higher  $d_{\text{pin}}$  leads to deeper dopant diffusion through the pinhole for B-doped poly-Si passivating contacts<sup>10</sup>. The data in Fig. 3e), 3b), and 3f) were obtained for a P-doped poly-Si layer with  $T_{\text{ann}} = 950^\circ\text{C}$  and  $d_{\text{pin}}$  of e) 2 nm, b) 5 nm, and f) 20 nm. These results show an increase in the radius of the regions with enhanced dopant diffusion with higher  $d_{\text{pin}}$ , confirming the conclusion reported by Feldmann et. al. in<sup>10</sup> also for P-doped poly-Si passivating contacts. The increase in the radius with  $d_{\text{pin}}$  is a result of

the dopants diffusing from a wider source than a point-like source as in the case of  $d_{\text{pin}} = 2 \text{ nm}$ <sup>10</sup>. Hence, this finding suggests that, assuming a certain scatter in  $d_{\text{pin}}$  values in real samples, radii of regions with local enhancement of dopant diffusion are also to be expected to have a certain variation, even within the same sample.

## 4 Study of Dopant Distribution under Poly-Si Passivating Contacts by SSRM

### 4.1 Poly-Si Passivating Contacts with Thermally Grown $\text{SiO}_x$ Films

Dopant distribution under poly-Si passivating contacts after the diffusion of dopants from the poly-Si film during annealing was investigated by SSRM for a broad set of samples, as summarized in Table 1. The results obtained on samples Imec-A, Imec-B, and Imec-C with a polished substrate, P-doped poly-Si, and thermal  $\text{SiO}_x$ , annealed at 900°C, 950°C, and 1050°C, are depicted in Fig. 4a)-c), respectively, where the logarithm of  $R$  is plotted for better visualization of regions with different doping levels. Far from the poly-Si passivating contact, the substrate has a uniform  $R$  corresponding to its uniform base resistivity. The passivating contact and the diffused region underneath typically feature a much lower  $R$  owing to the much higher doping levels there by a few orders of magnitude. It is noteworthy that the  $\text{SiO}_x$  layer cannot be resolved by SSRM and the  $R$  values in the poly-Si region are co-determined by not only the doping level but also the carrier mobility, which is typically lower than that of similarly doped c-Si.

Several conclusions can be drawn based on the  $R$  maps in Fig. 4a)-c). First, higher  $T_{\text{ann}}$  leads to deeper diffusion of dopants into the substrate as expected, indicated by the extended depth of the region with reduced  $R$  in the substrate. Interestingly, a comparison with Table 2 reveals that for Imec-A with non-Ohmic contacts only a very shallow diffusion ( $\sim 130 \text{ nm}$ ) is evident from Fig. 4a), while for Imec-C with poor passivation a very deep diffusion ( $\sim 1200 \text{ nm}$ ) is observed in Fig. 4c). These results indicate that the dopant diffusion into the substrate can influence the properties of poly-Si passivating contacts. Moderate diffusion is known to enhance tunneling by better band alignment and thereby yield lower  $\rho_c$ , while extreme diffusion can lead to excessive Auger recombination losses in the diffused region, thus lowering the passivation quality<sup>40</sup>. Moreover, the deep diffusion in Fig. 4c) is likely a result of the  $\text{SiO}_x$  film breaking up heavily given the high  $T_{\text{ann}} = 1050^\circ\text{C}$ , which probably damaged the passivation and contributed to the high  $J_0$ <sup>8</sup>. By contrast, the diffusion is more moderate in sample Imec-B

as shown in Fig. 4b), which probably is the reason for Imec-B having the optimal combination of  $J_0$  and  $\rho_c$  among the samples Imec-A-C, as Table 2 shows.

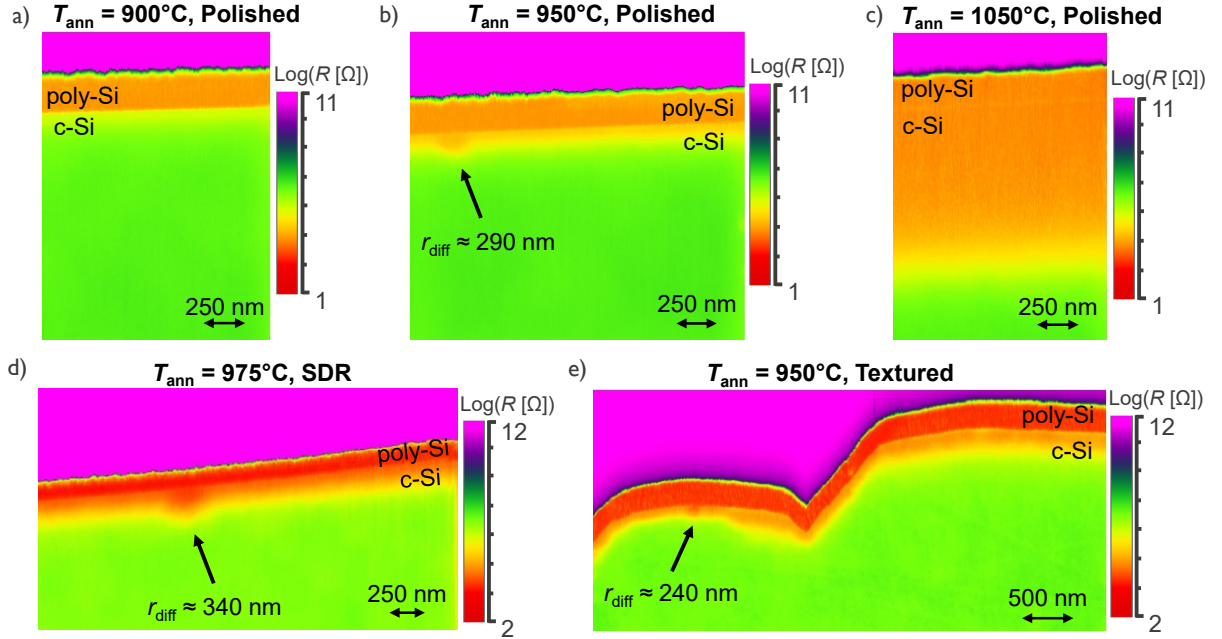


Figure 4. 2D maps of the logarithm of resistance ( $R$ ) measured by SSRM on samples with thermal  $\text{SiO}_x$ . a) Sample Imec-A with polished surface, annealed at 900°C. b) Sample Imec-B with polished surface, annealed at 950°C. c) Sample Imec-C with polished surface, annealed at 1050°C. d) Sample CEA with SDR surface, annealed at 975°C. e) Sample Imec-D with textured surface, annealed at 950°C. The black arrows indicate regions with enhanced dopant diffusion. The approximate radii of these regions ( $r_{\text{diff}}$ ) are also shown.

More interestingly, a semicircular region with locally enhanced dopant diffusion is detected in Fig. 4b) as indicated by the black arrow, which reasonably matches the theoretically expected distribution of dopants under a pinhole in the  $\text{SiO}_x$  film, as shown in Fig. 3. This result supports the finding of spatial doping non-uniformities under poly-Si passivating contacts by SKPM<sup>29</sup>. While it is not possible to prove the existence of a pinhole above the detected region due to the limited resolution of SSRM, certain indicators for the presence of the pinhole can still be found. First,  $r_{\text{diff}}$  of the region in Fig. 4b) is  $\sim 290$  nm, which matches well with the radius of the simulated region of enhanced diffusion in Fig. 3b), equal to  $\sim 300$  nm, obtained with a model similar to the structure of sample Imec-B and the same  $T_{\text{ann}}$  of 950°C. Moreover, it has been shown by temperature-dependent  $\rho_c$  measurements that in sample Imec-B, the dominant mechanism of charge carrier transport across the passivating contact is drift-diffusion via pinholes, which suggests the presence of pinholes in the  $\text{SiO}_x$ <sup>21</sup>. Based on these considerations, the region found in Fig. 4b) is attributed to enhanced dopant diffusion through a pinhole in the  $\text{SiO}_x$  film. It is important to note that such regions were not observed on a single occasion but on multiple  $R$  maps acquired on sample Imec-B. It is also interesting that no regions with local

enhancement are present in Fig. 4c) despite the higher  $T_{\text{ann}}$  of 1050°C, based on which a higher pinhole density would be expected. This can be explained by the  $\text{SiO}_x$  layer breaking up heavily in Imec-C as discussed above, yielding large areas without  $\text{SiO}_x$ . In that case, enhancement of dopant diffusion through regions where  $\text{SiO}_x$  is missing would not be localized; such regions would merge.

The  $R$  maps in Fig. 4d) and 4e) also reveal regions with local enhancement of diffusion on sample CEA with an SDR substrate, annealed at  $T_{\text{ann}} = 975^\circ\text{C}$  (Fig. 4d)), and on sample Imec-D with a textured substrate, annealed at  $T_{\text{ann}} = 950^\circ\text{C}$  (Fig. 4e)). These results show that local enhancement of diffusion can be observed (i) on samples originating from different laboratories and (ii) on substrates with rougher and industrially more relevant surface morphologies as well, without a significant change in the density of the regions. A slightly higher  $r_{\text{diff}}$  of 340 nm is found for sample CEA compared to Imec-B, which can be attributed to the slightly higher  $T_{\text{ann}}$ .

Comparing Fig. 4b) and 4e), corresponding to samples Imec-B and Imec-D, which were identically structured and processed except for the substrate surface morphology being polished and textured, respectively, reveals that only one region with enhanced diffusion is found on both samples, albeit for a scan area which is 2 times as large in case of the textured sample. This indicates that the density of the regions, and thus most probably the density of pinholes, do not increase or change significantly with rougher surfaces. This observation agrees with the finding in the literature that the dominant carrier transport mechanism across P-doped poly-Si passivating contacts remains unchanged when the surface morphology is altered, which suggests similar pinhole densities for polished and textured surface morphologies<sup>21</sup>. Moreover, non-uniformities in the depth of dopant diffusion in a less localized manner are evident from Fig. 4e) for the textured sample. This is not attributed to the presence of pinholes but can be explained with  $t_{\text{ox}}$  being less uniform on textured surfaces, which has been reported to be the case in the literature<sup>41</sup>. It is important to note that, based on studies on passivation quality<sup>5</sup>, the impact of surface morphology on passivating contact properties including the dopant distribution can be different for P and B doping, and the aforementioned conclusions may not be extended to the case of B-doped poly-Si passivating contacts without further tests, which are not covered in this work.

Another indicator of dopant diffusion via pinholes being the reason for the observed regions with enhanced doping is found by analyzing the  $R$  map in Fig. 5, acquired by measuring sample



ISE with a polished surface, P-doped poly-Si, thermal SiO<sub>x</sub> with  $t_{\text{ox}} = 1.2$  nm, and  $T_{\text{ann}} = 900^\circ\text{C}$ . In this image of 3  $\mu\text{m}$  width, 6 regions with enhanced diffusion are present as indicated by the black arrows. These regions were identified by the method described in Fig. 2d). A second image on a separate location of sample ISE was also acquired, where 5 regions were found within the 3  $\mu\text{m}$  wide image, confirming that a significant number of regions with enhanced doping are present in the  $R$  maps of sample ISE. From these data, the areal density of the regions with enhanced doping can be estimated to be in the range of  $2.8 \cdot 10^8$  to  $4 \cdot 10^8$  cm<sup>-2</sup>, which agrees well with the pinhole density determined by the selective TMAH etch method introduced by Wietler et. al. in <sup>23</sup>, and reported as  $4 \cdot 10^8$  cm<sup>-2</sup> <sup>36</sup>. This provides further evidence that the regions of enhanced dopant diffusion are most likely the result of diffusion via pinholes.

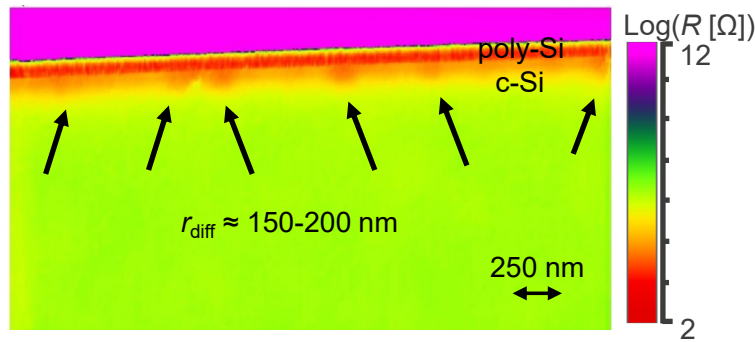


Figure 5. 2D map of the logarithm of resistance ( $R$ ) measured by SSRM on sample ISE with polished surface and 1.2 nm thick thermal SiO<sub>x</sub>, annealed at  $900^\circ\text{C}$ . The black arrows indicate regions with enhanced dopant diffusion. The range of radii of these regions ( $r_{\text{diff}}$ ) is also shown.

The fact that more regions are observed in Fig. 5 than in Fig. 4b) despite the lower  $T_{\text{ann}}$  of  $900^\circ\text{C}$  is attributed to the lower  $t_{\text{ox}}$  of 1.2 nm compared to 1.5 nm, which has been shown in the literature to have a strong impact on the pinhole density <sup>36</sup>. The significantly lower  $r_{\text{diff}}$  in Fig. 5 compared to Fig. 4b) is a result of the lower  $T_{\text{ann}}$ , which is expected based on the simulation results in Fig. 3. It is also noteworthy that all  $r_{\text{diff}}$  values in Fig. 4 and 5 agree with the width of such regions determined by SKPM as  $< 500$  nm <sup>29</sup>. By contrast, the depth of the regions was estimated by SKPM as  $> 200$  nm <sup>29</sup>, which is not the case in Fig. 5, even though a deeper diffusion would be expected in sample ISE with its lower  $t_{\text{ox}}$  and higher  $T_{\text{ann}}$  ( $t_{\text{ox}} = 1.5$  nm and  $T_{\text{ann}} = 850^\circ\text{C}$  in Kale et. al. <sup>29</sup>).

In addition to samples with 1.2-1.5 nm thick SiO<sub>x</sub>, the SSRM study was also extended to samples with SiO<sub>x</sub> films thicker than 2 nm, annealed at sufficiently high  $T_{\text{ann}} > 1000^\circ\text{C}$  to create pinholes in such thick SiO<sub>x</sub> layers <sup>21</sup>. This is because tunneling through SiO<sub>x</sub> is negligible with

such thick  $\text{SiO}_x$  films and drift-diffusion via pinholes is the dominant mechanism of charge carrier transport across these passivating contacts<sup>20,21</sup>. In fact, the pinhole transport model was originally developed to describe the properties of samples with  $t_{\text{ox}} > 2 \text{ nm}$ <sup>7</sup>. For this purpose, 2D  $R$  maps were acquired on samples ISFH-A (Fig. 6a)) and ISFH-B (Fig. 6b)) with polished surface, 2.2 nm thick thermal  $\text{SiO}_x$ , and  $T_{\text{ann}} = 1035^\circ\text{C}$ . These samples differ only in the type of dopant used for doping the poly-Si film, which is P in ISFH-A and B in ISFH-B. The  $R$  maps in Fig. 6 reveal a few interesting properties. First, dopant diffusion is very deep across the whole  $R$  maps, extending  $\sim 1 \text{ }\mu\text{m}$  into the substrate, similar to sample Imec-C in Fig. 4c), which was also annealed at a high  $T_{\text{ann}}$  of  $1050^\circ\text{C}$ . However, unlike in Imec-C, the thicker  $\text{SiO}_x$  films in ISFH-A and ISFH-B are not expected to be broken up heavily, since excellent passivation was achieved with both ISFH samples as shown by the low  $J_0$  values in Table 2. Moreover, for similarly processed samples, moderate pinhole density values of  $1.1 \cdot 10^8 \text{ cm}^{-2}$  and  $1.6 \cdot 10^8 \text{ cm}^{-2}$  were reported in the literature based on the selective TMAH etch method, revealing the presence of pinholes but no excessive balling up in the  $\text{SiO}_x$ <sup>23</sup>.

Secondly, regions with enhanced dopant diffusion are also detected in samples with thicker  $\text{SiO}_x$ , but only for the P-doped and not the B-doped sample. These regions are not easily discernible from the 2D  $R$  maps in Fig. 6a) and 6b) due to the deep dopant diffusion mentioned above. Therefore, 1D horizontal profiles of  $R$  acquired at the locations indicated by the dotted arrows in Fig. 6a) and 6b), respectively, are depicted in Fig. 6c). It is clear from Fig. 6c) that two regions with locally enhanced P diffusion are found in ISFH-A, while no region with enhanced B diffusion is found in ISFH-B, even though the presence of pinholes had been experimentally shown for both samples<sup>23</sup>. The findings of the simulation study in Fig. 3d) for the case of B doping supports the results of Fig. 6b) in that the region with enhanced doping under pinholes is hardly distinguishable from those far from the pinholes, where dopant diffusion happens through the intact  $\text{SiO}_x$ , due to the aforementioned smaller difference between B diffusivities in the  $\text{SiO}_x$  and Si. On the other hand, the regions with locally enhanced doping in Fig. 6a), while distinguishable in the value of the measured  $R$ , are also similarly buried and do not extend deeper into the substrate than the uniform highly doped region. This observation is not supported by the simulation result in Fig. 3c), which predicts a significantly deeper diffusion of P via the pinhole than through the  $\text{SiO}_x$  film. The reason for this disagreement between the simulation and experimental results is not well-understood and requires further investigation.

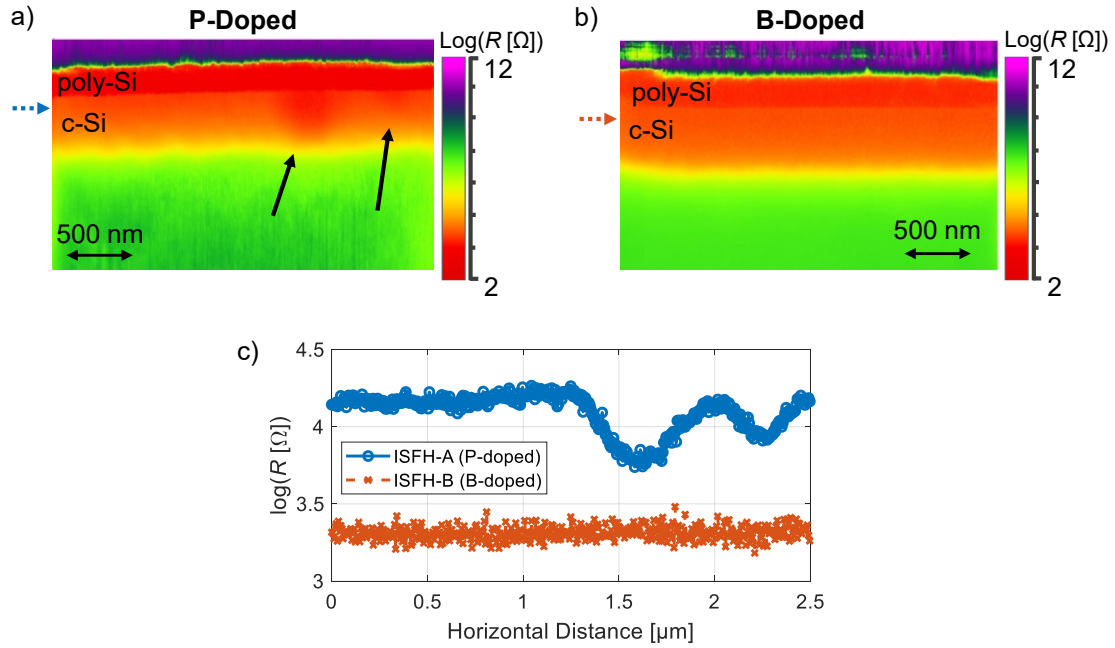


Figure 6. Logarithm of resistance ( $R$ ) measured by SSRM on samples with polished surface, 2.2 nm thick thermal  $\text{SiO}_x$ , and annealing temperature of  $1035^\circ\text{C}$ . a) 2D map of sample ISFH-A with phosphorus (P) doping in the poly-Si film. The black arrows indicate regions with enhanced dopant diffusion. The dotted blue arrow indicates where a horizontal 1D profile of  $R$  was extracted for c). b) 2D map of sample ISFH-B with boron (B) doping in the poly-Si film. The dotted orange arrow indicates where a horizontal 1D profile of  $R$  was extracted for c). c) Horizontal 1D profiles calculated as the average of 5 scans acquired at the locations indicated by the dotted blue (in a)) and orange (in b)) arrows.

For samples ISFH-A and ISFH-B, quantitative analysis of the SSRM results was also performed by converting the  $R$  maps into  $N_{\text{act}}$  maps. In Fig. 7a), 1D profiles of  $N_{\text{D,act}}$  inside and outside the regions with enhanced dopant diffusion in ISFH-A are shown, while in Fig. 7b), a 1D profile of  $N_{\text{A,act}}$  in ISFH-B is plotted. For comparison, 1D profiles of  $N_{\text{act}}$  obtained by ECV as well as TCAD simulations are also shown in Fig. 7. The SSRM profiles in Fig. 7a) indicate that, inside the region with doping enhancement, dopant diffusion is slightly deeper and the peak  $N_{\text{D,act}}$  in the substrate appears to increase by  $\sim 2.5$  times, from  $6 \cdot 10^{17} \text{ cm}^{-3}$  to  $1.5 \cdot 10^{18} \text{ cm}^{-3}$ , compared to the profile outside the region with enhanced doping. The peak  $N_{\text{D,act}}$  value in the substrate determined by ECV equals  $\sim 3 \cdot 10^{18} \text{ cm}^{-3}$ , which agrees well with the corresponding simulated peak  $N_{\text{D,act}}$  value. This is expected since the simulated profile was extracted in a region with intact  $\text{SiO}_x$ , far removed from pinholes, and ECV probes a large area ( $\sim 1 \text{ cm}^2$ ) where the  $\text{SiO}_x$  film was mostly intact given the moderate pinhole densities in sample ISFH-A<sup>23</sup>. The disagreement between the SSRM and ECV results is significant and was found to be even greater for some of the other samples with P-doped poly-Si passivating contacts (results not shown here). Therefore, the data acquired by SSRM on samples with P doping are assessed only qualitatively in this work. We speculate that the observed discrepancy is a result

of an unexpected, high back contact resistance of the SSRM samples, which led to the overestimation of the spreading resistance and therefore the underestimation of the calculated  $N_{D,act}$ . This problem can be potentially solved by preparing the back contact of SSRM samples using a metal with a more suitable work function for contacting P-doped Si, which will be investigated as part of our future work. The assumed high back contact resistance can also explain that SSRM significantly underestimates  $N_{D,act}$  in the poly-Si film compared to ECV. A smaller mismatch between the simulated  $N_{D,act}$  and the ECV data in the poly-Si is also found in Fig. 7a), which suggests that the model of phosphorus activation in the simulated poly-Si film needs to be improved.

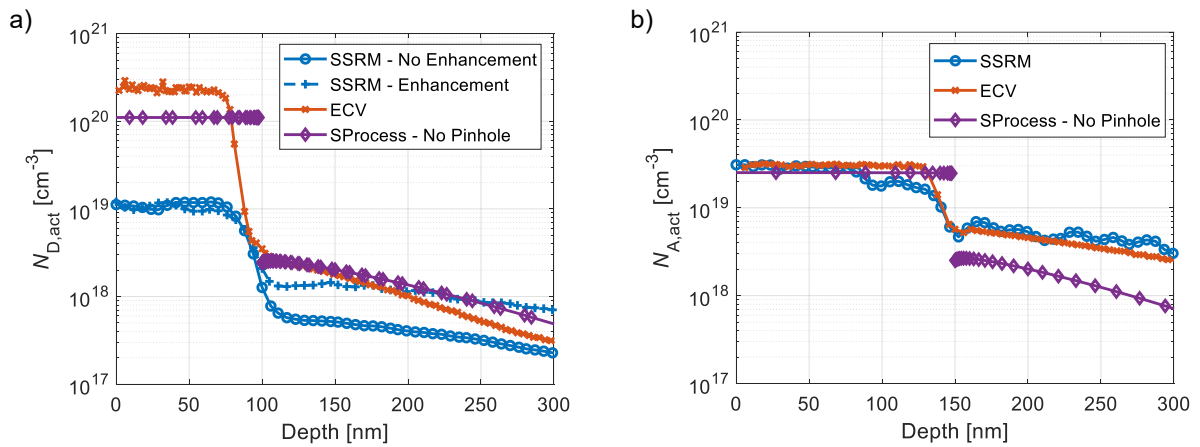


Figure 7. 1D profiles of the active dopant concentration ( $N_{D,act}$  or  $N_{A,act}$ ) measured by SSRM and ECV, as well as simulated with Sentaurus Process (denoted SProcess in the figure legends), on samples with polished surface, 2.2 nm thick thermal  $\text{SiO}_x$ , and annealing temperature of 1035°C. a) Sample ISFH-A with phosphorus (P) doping in the poly-Si film. 1D profiles determined by SSRM were extracted both inside and outside regions with local enhancement of dopant diffusion. b) Sample ISFH-B with boron (B) doping in the poly-Si film.

By contrast, Fig. 7b) shows that the  $N_{A,act}$  data in the poly-Si film of sample ISFH-B with the B-doped passivating contact determined by SSRM, ECV, and TCAD simulations are in excellent agreement. Moreover, the agreement between the SSRM and ECV data also holds for the diffused region in the substrate, with the peak  $N_{A,act}$  value there being  $\sim 5 \cdot 10^{18} \text{ cm}^{-3}$ . While the corresponding simulated  $N_{A,act}$  in the substrate is 50% lower, this is probably a result of the parameterization of B diffusivity in the  $\text{SiO}_x$  layer not being sufficiently accurate. The matching data from SSRM and ECV indicate that the back contact resistance of the SSRM sample is negligible in case of B-doped passivating contacts, enabling the quantification of the SSRM results. This motivates extending the study to other B-doped samples in the future, since ISFH-B is the only B-doped sample investigated in this work and does not show any regions with enhanced doping to analyze quantitatively.

## 4.2 Poly-Si Passivating Contacts with Wet-Chemically Grown SiO<sub>x</sub> Films

Along with thermal oxidation, wet-chemical approaches are the most utilized techniques to fabricate the interfacial SiO<sub>x</sub> film in poly-Si passivating contacts. Therefore, the SSRM study was extended to samples with wet-chemically grown SiO<sub>x</sub> films, albeit not as systematically as for samples with thermal SiO<sub>x</sub>. Two samples, ISFH-C and ISC, with SDR substrates, P-doped poly-Si films, and wet-chemically grown SiO<sub>x</sub> were investigated by SSRM, and the resulting  $R$  maps are depicted in Fig. 8a) and 8b), respectively. We would like to note that the samples differ in a few important design and process parameters. The SiO<sub>x</sub> film of ISFH-C was grown in ozonated deionized water (H<sub>2</sub>O:O<sub>3</sub>), has a  $t_{\text{ox}}$  of 1.7 nm, and was annealed at 840°C, while for ISC, SiO<sub>x</sub> was grown in concentrated nitric acid (HNO<sub>3</sub>) with a  $t_{\text{ox}}$  of 1.4 nm, and  $T_{\text{ann}}$  was 825°C. Both samples were prepared using optimized process flows and yield low  $J_0$  and  $\rho_c$  values simultaneously, as Table 2 shows.

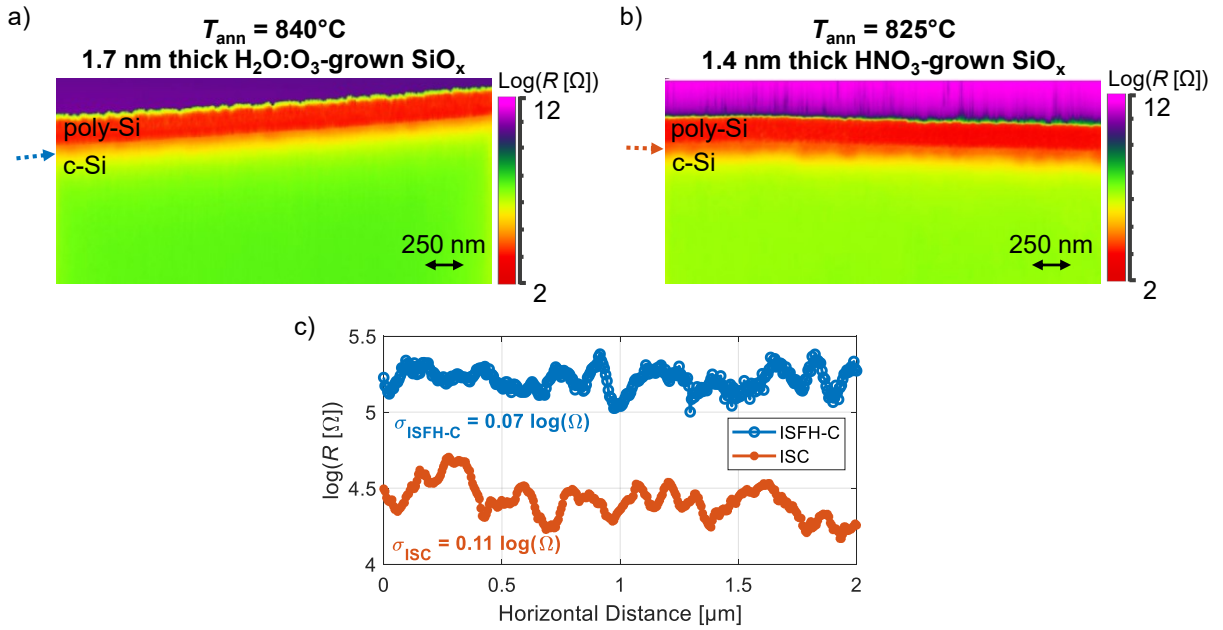


Figure 8. Logarithm of resistance ( $R$ ) measured by SSRM on samples with wet-chemically grown SiO<sub>x</sub>. a) 2D map of sample ISFH-C with a 1.7 nm thick SiO<sub>x</sub> film grown in ozonated deionized water, annealed at 840°C. The dotted blue arrow indicates where a horizontal 1D profile of  $R$  was extracted for c). b) 2D map of sample ISC with a 1.4 nm thick SiO<sub>x</sub> film grown in nitric acid, annealed at 825°C. The dotted orange arrow indicates where a horizontal 1D profile of  $R$  was extracted for c). c) Horizontal 1D profiles calculated as the average of 5 scans acquired at the locations indicated by the dotted blue (in a)) and orange (in b)) arrows. Standard deviation ( $\sigma$ ) values of both 1D profiles are also indicated on the graph.

It is evident from the images in Fig. 8 that protruding regions with enhanced doping are not present in the samples with wet-chemical SiO<sub>x</sub> films. Nevertheless, non-uniformities in the diffused region under the passivating contact are clearly discernible, particularly in the  $R$  map of sample ISC in Fig. 8b). It is unlikely that these features result from a very high pinhole

density, given the low  $J_0$  achieved with these samples, as seen in Table 2. Instead, the non-uniformities can be explained if a poorer thickness homogeneity is assumed for wet-chemical  $\text{SiO}_x$  films compared to thermal  $\text{SiO}_x$  films, which would lead to a slight enhancement of dopant diffusion in regions where the  $\text{SiO}_x$  film is thinner. This assumption is reasonable, since experimental evidence of thickness inhomogeneities in wet-chemical  $\text{SiO}_x$  films is present in the literature<sup>24,42,43</sup>.

The non-uniformities in the dopant distribution are less evident in Fig. 8a) than in Fig. 8b). This is more clearly observed by analyzing the 1D horizontal profiles of  $R$  shown in Fig. 8c), acquired at the locations indicated by the dotted arrows in Fig. 8a) and 8b), respectively. The profile of sample ISC exhibits a  $\sigma$  value equal to  $0.11 \log(\Omega)$ , which is  $\sim 57\%$  higher than that of sample ISFH-C. The higher non-uniformities in case of sample ISC might be a result of the slightly lower  $t_{\text{ox}}$  or the different wet-chemical oxidation technique used, which might have yielded a different level of the homogeneity of  $t_{\text{ox}}$ . Overall, a more systematic study is necessary for better understanding the impact of various sample design and process parameters on the dopant distribution under poly-Si passivating contacts with wet-chemical  $\text{SiO}_x$  films.

## 5 Summary and Outlook

Understanding the properties and the working mechanism of poly-Si passivating contacts requires accurately modeling the transport of charge carriers across the interfacial  $\text{SiO}_x$  film in the passivating contact. Such models need to account for two relevant carrier transport mechanisms: tunneling through the  $\text{SiO}_x$  film and drift-diffusion via pinholes in the  $\text{SiO}_x$  film. An important parameter for the transport via pinholes is the distribution of dopants in the vicinity of pinholes. The dopant distribution under poly-Si passivating contacts and, in particular, under the pinholes therein is studied in this work by simulations and experiments.

Using the Sentaurus Process software, the annealing process typically applied to poly-Si passivating contacts was simulated utilizing a 2D model of the passivating contact with a pinhole in the  $\text{SiO}_x$  layer. The simulations showed that dopant diffusion is locally enhanced in a semicircular region under the pinhole. The radius of the region increases with  $T_{\text{ann}}$  and  $d_{\text{pin}}$ . Moreover, the radius is lower for B-doped poly-Si compared to P-doped poly-Si.

The experimental study was performed using the SSRM technique which provides 2D  $R$  maps of the passivating contacts. This investigation confirmed the presence of semicircular regions

with enhanced dopant diffusion under poly-Si passivating contacts experimentally. While direct proof of the presence of pinholes above the regions with enhanced diffusion could not be achieved by SSRM, it was found that the regions appear in samples where pinholes had been detected by other methods. In one of the samples, the densities of the regions with enhanced diffusion and pinholes were found to match.

The regions with locally enhanced diffusion were detected in multiple samples. In samples with thermally grown  $\text{SiO}_x$  and P-doped poly-Si, the regions were observed for  $T_{\text{ann}} = 900\text{-}975^\circ\text{C}$  in case of  $t_{\text{ox}} = 1.2\text{-}1.5$  nm, and for  $T_{\text{ann}} = 1035^\circ\text{C}$  in case of  $t_{\text{ox}} = 2.2$  nm. Using a polished or textured substrate did not change the density of the regions significantly, but, in case of the textured substrate, dopant diffusion through the  $\text{SiO}_x$  was non-uniform in a less localized manner, probably due to  $t_{\text{ox}}$  being inhomogeneous. In case of B-doped poly-Si and  $T_{\text{ann}} = 1035^\circ\text{C}$ , no regions of enhanced diffusion under the pinholes were found in contrast to P-doped poly-Si. This is attributed to similar B diffusivity through the interfacial  $\text{SiO}_x$  and via the pinholes, yielding a negligible diffusion enhancement under the pinholes. When wet-chemically grown  $\text{SiO}_x$  films were used in the passivating contacts instead of thermal  $\text{SiO}_x$ , less distinct non-uniformities were observed in the distribution of dopants under the passivating contact. The non-uniformities are attributed to poor  $t_{\text{ox}}$  homogeneity in case of wet-chemical  $\text{SiO}_x$  films, leading to a high number of regions with slight enhancement in dopant diffusion.

The presented findings improve the understanding of the properties of poly-Si passivating contacts and motivate further studies by SSRM. The focus of future work will be to systematically study B-doped passivating contacts, as well as passivating contacts with wet-chemical  $\text{SiO}_x$  films. Moreover, problems encountered when converting the  $R$  data to  $N_{\text{act}}$  will be further investigated to enable the quantitative analysis of the SSRM results.

### Supporting Information

Supporting Information: Additional details regarding experimental sample properties and contact resistivity measurements.

### Author Information

\*Corresponding author: meric.firat@student.kuleuven.be

## Author Contributions

The manuscript was written through contributions of all authors. All authors have given approval to the final version of the manuscript.

## Funding Sources

This work was supported by the European Union's Horizon2020 Programme for research, technological development, and demonstration [grant number 857793]; and by the Kuwait Foundation for the Advancement of Sciences [grant number CN18-15EE-01].

## Acknowledgments

The authors would like to acknowledge Laura Galleni from KU Leuven for her help with sample preparation, An De Keersgieter from Imec for the valuable discussions about the Sentaurus TCAD simulations, and Christina Hollemann from ISFH for the scientific support she provided for the work.

## References

- (1) Yan, D.; Cuevas, A.; Michel, J. I.; Zhang, C.; Wan, Y.; Zhang, X.; Bullock, J. Polysilicon Passivated Junctions: The next Technology for Silicon Solar Cells? *Joule* **2021**, 5 (4), 811–828. <https://doi.org/10.1016/j.joule.2021.02.013>.
- (2) Haase, F.; Hollemann, C.; Schäfer, S.; Merkle, A.; Rienäcker, M.; Krügener, J.; Brendel, R.; Peibst, R. Laser Contact Openings for Local Poly-Si-Metal Contacts Enabling 26.1%-Efficient POLO-IBC Solar Cells. *Sol. Energy Mater. Sol. Cells* **2018**, 186, 184–193. <https://doi.org/10.1016/j.solmat.2018.06.020>.
- (3) Feldmann, F.; Mack, S.; Steinhauser, B.; Tutsch, L.; Polzin, J.-I.; Temmler, J.; Moldovan, A.; Wolf, A.; Rentsch, J.; Hermle, M.; Glunz, S. W. Towards Industrial Manufacturing of TOPCon. *Photovoltaics International*. 2018, pp 46–55.
- (4) Chen, R.; Zheng, P.; Wright, M.; Chen, D.; Yang, J.; Ciesla, A.; Wenham, S. 24.58% Efficient Commercial n-Type Silicon Solar Cells with Hydrogenation. *Prog. Photovoltaics Res. Appl.* **2021**, 1–6. <https://doi.org/10.1002/pip.3464>.
- (5) Schmidt, J.; Peibst, R.; Brendel, R. Surface Passivation of Crystalline Silicon Solar Cells: Present and Future. *Sol. Energy Mater. Sol. Cells* **2018**, 187, 39–54. <https://doi.org/10.1016/j.solmat.2018.06.047>.
- (6) Peibst, R.; Römer, U.; Larionova, Y.; Rienäcker, M.; Merkle, A.; Folchert, N.; Reiter, S.; Turcu, M.; Min, B.; Krügener, J.; Tetzlaff, D.; Bugiel, E.; Wietler, T.; Brendel, R. Working Principle of Carrier Selective Poly-Si/c-Si Junctions: Is Tunnelling the Whole



- Story? *Sol. Energy Mater. Sol. Cells* **2016**, *158*, 60–67. <https://doi.org/10.1016/j.solmat.2016.05.045>.
- (7) Peibst, R.; Römer, U.; Hofmann, K. R.; Lim, B.; Wietler, T. F.; Krügener, J.; Harder, N. P.; Brendel, R. A Simple Model Describing the Symmetric I-V Characteristics of p Polycrystalline Si/n Monocrystalline Si, and n Polycrystalline Si/p Monocrystalline Si Junctions. *IEEE J. Photovoltaics* **2014**, *4* (3), 841–850. <https://doi.org/10.1109/JPHOTOV.2014.2310740>.
  - (8) Feldmann, F.; Nogay, G.; Löper, P.; Young, D. L.; Lee, B. G.; Stradins, P.; Hermle, M.; Glunz, S. W. Charge Carrier Transport Mechanisms of Passivating Contacts Studied by Temperature-Dependent J-V Measurements. *Sol. Energy Mater. Sol. Cells* **2018**, *178*, 15–19. <https://doi.org/10.1016/j.solmat.2018.01.008>.
  - (9) Kamins, T. *Polycrystalline Silicon for Integrated Circuits and Displays*; Springer US, 1998. <https://doi.org/10.1007/978-1-4615-5577-3>.
  - (10) Feldmann, F.; Schön, J.; Niess, J.; Lerch, W.; Hermle, M. Studying Dopant Diffusion from Poly-Si Passivating Contacts. *Sol. Energy Mater. Sol. Cells* **2019**, *200*. <https://doi.org/10.1016/j.solmat.2019.109978>.
  - (11) Liu, W.; Yang, X.; Kang, J.; Li, S.; Xu, L.; Zhang, S.; Xu, H.; Peng, J.; Xie, F.; Fu, J. H.; Wang, K.; Liu, J.; Alzahrani, A.; De Wolf, S. Polysilicon Passivating Contacts for Silicon Solar Cells: Interface Passivation and Carrier Transport Mechanism. *ACS Appl. Energy Mater.* **2019**, *2* (7), 4609–4617. <https://doi.org/10.1021/acsaem.8b02149>.
  - (12) Wolstenholme, G. R.; Jorgensen, N.; Ashburn, P.; Booker, G. R. An Investigation of the Thermal Stability of the Interfacial Oxide in Polycrystalline Silicon Emitter Bipolar Transistors by Comparing Device Results with High-Resolution Electron Microscopy Observations. *J. Appl. Phys.* **1987**, *61* (1), 225–233. <https://doi.org/10.1063/1.338861>.
  - (13) Lancaster, K.; Großer, S.; Feldmann, F.; Naumann, V.; Hagendorf, C. Study of Pinhole Conductivity at Passivated Carrier-Selected Contacts of Silicon Solar Cells. In *Energy Procedia*; Elsevier Ltd, 2016; Vol. 92, pp 116–121. <https://doi.org/10.1016/j.egypro.2016.07.040>.
  - (14) Kale, A. S.; Nemeth, W.; Guthrey, H.; Kennedy, E.; Norman, A. G.; Page, M.; Al-Jassim, M.; Young, D. L.; Agarwal, S.; Stradins, P. Understanding the Charge Transport Mechanisms through Ultrathin SiO<sub>x</sub> Layers in Passivated Contacts for High-Efficiency Silicon Solar Cells. *Appl. Phys. Lett.* **2019**, *114* (8). <https://doi.org/10.1063/1.5081832>.
  - (15) Guthrey, H.; Lima Salles, C.; Kale, A. S.; Nemeth, W.; Page, M.; Agarwal, S.; Young, D. L.; Al-Jassim, M.; Stradins, P. Effect of Surface Texture on Pinhole Formation in

- SiO X-Based Passivated Contacts for High-Performance Silicon Solar Cells. *ACS Appl. Mater. Interfaces* **2020**, *12* (50), 55737–55745. <https://doi.org/10.1021/acsami.0c12795>.
- (16) Würfel, U.; Cuevas, A.; Würfel, P. Charge Carrier Separation in Solar Cells. *IEEE J. Photovoltaics* **2015**, *5* (1), 461–469. <https://doi.org/10.1109/JPHOTOV.2014.2363550>.
  - (17) Melskens, J.; Van De Loo, B. W. H.; Macco, B.; Black, L. E.; Smit, S.; Kessels, W. M. M. Passivating Contacts for Crystalline Silicon Solar Cells: From Concepts and Materials to Prospects. *IEEE J. Photovoltaics* **2018**, *8* (2), 373–388. <https://doi.org/10.1109/JPHOTOV.2018.2797106>.
  - (18) Brendel, R.; Peibst, R. Contact Selectivity and Efficiency in Crystalline Silicon Photovoltaics. *IEEE J. Photovoltaics* **2016**, *6* (6), 1413–1420. <https://doi.org/10.1109/JPHOTOV.2016.2598267>.
  - (19) Post, I. R. C.; Ashbum, P.; Wolstenholme, G. R. Polysilicon Emitters for Bipolar Transistors : A Review and Re-Evaluation of Theory and Experiment. *IEEE Trans. Electron Devices* **1992**, *39* (7), 1717–1731. <https://doi.org/10.1109/16.141239>.
  - (20) Folchert, N.; Rienäcker, M.; Yeo, A. A.; Min, B.; Peibst, R.; Brendel, R. Temperature-Dependent Contact Resistance of Carrier Selective Poly-Si on Oxide Junctions. *Sol. Energy Mater. Sol. Cells* **2018**, *185*, 425–430. <https://doi.org/10.1016/j.solmat.2018.05.046>.
  - (21) Galleni, L.; Firat, M.; Radhakrishnan, H. S.; Duerinckx, F.; Tous, L.; Poortmans, J. Mechanisms of Charge Carrier Transport in Polycrystalline Silicon Passivating Contacts. *Sol. Energy Mater. Sol. Cells* **2021**, *232* (September), 111359. <https://doi.org/10.1016/j.solmat.2021.111359>.
  - (22) Gan, J. Y.; Swanson, R. M. Polysilicon Emitters for Silicon Concentrator Solar Cells. In *Proceedings of IEEE 21st Photovoltaic Specialists Conference (PVSC)*; 1990; pp 245–250.
  - (23) Wietler, T. F.; Tetzlaff, D.; Krügener, J.; Rienäcker, M.; Haase, F.; Larionova, Y.; Brendel, R.; Peibst, R. Pinhole Density and Contact Resistivity of Carrier Selective Junctions with Polycrystalline Silicon on Oxide. *Appl. Phys. Lett.* **2017**, *110* (25). <https://doi.org/10.1063/1.4986924>.
  - (24) Feldmann, F.; Nogay, G.; Polzin, J. I.; Steinhauser, B.; Richter, A.; Fell, A.; Schmiga, C.; Hermle, M.; Glunz, S. W. A Study on the Charge Carrier Transport of Passivating Contacts. *IEEE J. Photovoltaics* **2018**, *8* (6), 1503–1509. <https://doi.org/10.1109/JPHOTOV.2018.2870735>.
  - (25) Campa, A.; Smole, F.; Folchert, N.; Wietler, T.; Min, B.; Brendel, R.; Topic, M. Detailed

- Analysis and Understanding of the Transport Mechanism of Poly-Si-Based Carrier Selective Junctions. *IEEE J. Photovoltaics* **2019**, *9* (6), 1575–1582. <https://doi.org/10.1109/JPHOTOV.2019.2943610>.
- (26) Younas, R.; Imran, H.; Shah, S. I. H.; Abdolkader, T. M.; Butt, N. Z. Computational Modeling of Polycrystalline Silicon on Oxide Passivating Contact for Silicon Solar Cells. *IEEE Trans. Electron Devices* **2019**, *66* (4), 1819–1826. <https://doi.org/10.1109/TED.2019.2900691>.
- (27) Folchert, N.; Peibst, R.; Brendel, R. Modeling Recombination and Contact Resistance of Poly-Si Junctions. *Prog. Photovoltaics Res. Appl.* **2020**, *28* (12) (March), 1289–1307. <https://doi.org/10.1002/pip.3327>.
- (28) Krügener, J.; Haase, F.; Hollemann, C.; Osten, H.-J.; Peibst, R. Dopant Diffusion through Pinholes and Continuous Oxide Layers in N-Type Polysilicon on Oxide (POLO) Passivating Contacts. In *29th Photovoltaic Science and Engineering Conference (PVSEC-29) - Xi'an, China; 2019*.
- (29) Kale, A. S.; Nanayakkara, S. U.; Nemeth, W.; Guthrey, H.; Page, M.; Al-Jassim, M.; Young, D. L.; Stradins, P.; Agarwal, S. *Scanning Kelvin Probe Microscopy: A Tool to Investigate Nano-Scale Doping Non-Uniformities in Poly-Si/SiO<sub>x</sub> Contacts: Preprint*; Golden, Colorado, United States, 2019.
- (30) Schulze, A.; Eyben, P.; Mody, J.; Paredis, K.; Wouters, L.; Celano, U.; Vandervorst, W. Mapping Conductance and Carrier Distributions in Confined Three-Dimensional Transistor Structures. In *Electrical Atomic Force Microscopy for Nanoelectronics*; 2019; pp 71–106. [https://doi.org/10.1007/978-3-030-15612-1\\_3](https://doi.org/10.1007/978-3-030-15612-1_3).
- (31) Fırat, M.; Sivaramakrishnan Radhakrishnan, H.; Recamán Payo, M.; Duerinckx, F.; Tous, L.; Poortmans, J. In Situ Phosphorus-Doped Polycrystalline Silicon Films by Low Pressure Chemical Vapor Deposition for Contact Passivation of Silicon Solar Cells. **2022**, *231* (September 2021), 78–87. <https://doi.org/10.1016/j.solener.2021.11.045>.
- (32) Hollemann, C.; Haase, F.; Rienäcker, M.; Barnscheidt, V.; Krügener, J.; Folchert, N.; Brendel, R.; Richter, S.; Großer, S.; Sauter, E.; Hübner, J.; Oestreich, M.; Peibst, R. Separating the Two Polarities of the POLO Contacts of an 26.1%-Efficient IBC Solar Cell. *Sci. Rep.* **2020**, *10* (1). <https://doi.org/10.1038/s41598-019-57310-0>.
- (33) Tetzlaff, D.; Krügener, J.; Larionova, Y.; Reiter, S.; Turcu, M.; Peibst, R.; Höhne, U.; Kähler, J. D.; Wietler, T. Evolution of Oxide Disruptions: The (W)Hole Story about Poly-Si/c-Si Passivating Contacts. In *Proceedings of IEEE 43rd Photovoltaic Specialists Conference (PVSC)*; IEEE, 2016; pp 221–224.

<https://doi.org/10.1109/PVSC.2016.7749582>.

- (34) Ghezzeo, M.; Brown, D. M. Diffusivity Summary of B, Ga, P, As, and Sb in SiO<sub>2</sub>. *J. Electrochem. Soc.* **1973**, *120* (1), 146. <https://doi.org/10.1149/1.2403391>.
- (35) Mastromatteo, M.; De Salvador, D.; Napolitani, E.; Arduca, E.; Seguíni, G.; Frascaroli, J.; Perego, M.; Nicotra, G.; Spinella, C.; Lenardi, C.; Carnera, A. Modeling of Phosphorus Diffusion in Silicon Oxide and Incorporation in Silicon Nanocrystals. *J. Mater. Chem. C* **2016**, *4* (16), 3531–3539. <https://doi.org/10.1039/c5tc04287a>.
- (36) Polzin, J. I.; Feldmann, F.; Steinhäuser, B.; Hermle, M.; Glunz, S. W. Study on the Interfacial Oxide in Passivating Contacts. In *AIP Conference Proceedings*; American Institute of Physics Inc., 2019; Vol. 2147. <https://doi.org/10.1063/1.5123843>.
- (37) Rienäcker, M.; Bossmeyer, M.; Merkle, A.; Römer, U.; Haase, F.; Krugener, J.; Brendel, R.; Peibst, R. Junction Resistivity of Carrier-Selective Polysilicon on Oxide Junctions and Its Impact on Solar Cell Performance. *IEEE J. Photovoltaics* **2017**, *7* (1), 11–18. <https://doi.org/10.1109/JPHOTOV.2016.2614123>.
- (38) Chaudhary, A.; Hoß, J.; Lossen, J.; Huster, F.; Kopecek, R.; van Swaaij, R.; Zeman, M. Influence of Polysilicon Thickness on Properties of Screen-Printed Silver Paste Metallized Silicon Oxide/Polysilicon Passivated Contacts. *Phys. Status Solidi Appl. Mater. Sci.* **2021**, *218* (18), 1–9. <https://doi.org/10.1002/pssa.202100243>.
- (39) Hantschel, T.; Tsigkourakos, M.; Zha, L.; Nuytten, T.; Paredis, K.; Majeed, B.; Vandervorst, W. Diamond Scanning Probes with Sub-Nanometer Resolution for Advanced Nanoelectronics Device Characterization. *Microelectron. Eng.* **2016**, *159*, 46–50. <https://doi.org/10.1016/j.mee.2016.02.053>.
- (40) Steinkemper, H.; Feldmann, F.; Bivour, M.; Hermle, M. Numerical Simulation of Carrier-Selective Electron Contacts Featuring Tunnel Oxides. *IEEE J. Photovoltaics* **2015**, *5* (5), 1348–1356. <https://doi.org/10.1109/JPHOTOV.2015.2455346>.
- (41) Kale, A. S.; Nemeth, W.; Guthrey, H.; Nanayakkara, S. U.; Lasalvia, V.; Theingi, S.; Findley, D.; Page, M.; Al-Jassim, M.; Young, D. L.; Stradins, P.; Agarwal, S. Effect of Crystallographic Orientation and Nanoscale Surface Morphology on Poly-Si/SiO<sub>x</sub> Contacts for Silicon Solar Cells. *ACS Appl. Mater. Interfaces* **2019**, *11* (45), 42021–42031. <https://doi.org/10.1021/acsami.9b11889>.
- (42) Choi, S.; Min, K. H.; Jeong, M. S.; Lee, J. I.; Kang, M. G.; Song, H. E.; Kang, Y.; Lee, H. S.; Kim, D.; Kim, K. H. Structural Evolution of Tunneling Oxide Passivating Contact upon Thermal Annealing. *Sci. Rep.* **2017**, *7* (1), 1–11. <https://doi.org/10.1038/s41598-017-13180-y>.

- (43) Moldovan, A.; Feldmann, F.; Zimmer, M.; Rentsch, J.; Benick, J.; Hermle, M. Tunnel Oxide Passivated Carrier-Selective Contacts Based on Ultra-Thin SiO<sub>2</sub> Layers. *Sol. Energy Mater. Sol. Cells* **2015**, *142*, 123–127. <https://doi.org/10.1016/j.solmat.2015.06.048>.

**For Table of Contents Only**

